

Regime Map and Triple Point in Selective Withdrawal

Zehao Pan¹, Janine K. Nunes¹, and Howard A. Stone^{1*}*Department of Mechanical and Aerospace Engineering, Princeton University, Princeton, New Jersey 08544, USA* (Received 20 September 2020; accepted 4 December 2020; published 31 December 2020)

Entrainment in selective withdrawal occurs when both the top and bottom phases are withdrawn through a capillary tube oriented perpendicular to a flat gravitationally separated liquid-liquid interface. The tube introduces two distinct features to the conditions for fluid entrainment. First, the ratio of the two phases being withdrawn is affected by the region of influence of the flow upstream of the tube's orifice. Second, a minimum withdrawal flow rate must be reached for entrainment regardless of the distance between the interface and the tube. We show that these phenomena can be understood based on the Reynolds number that governs the external flow field around the capillary tube and the capillary number that regulates the effect of the viscosity and capillarity.

DOI: [10.1103/PhysRevLett.125.264502](https://doi.org/10.1103/PhysRevLett.125.264502)

Selective withdrawal occurs when a sink flow is present near a stratified fluid-fluid interface. In an immiscible fluid system, the sink flow causes the interface between the fluids to deform until entrainment of both of the fluids occurs given sufficient withdrawal strength. Near the onset of entrainment, the interface can form a self-similar hump or tip [1–5]; during entrainment the interface forms a thin spout [6] following a saddle-node bifurcation transition, as suggested by numerical simulations [7]. The structure that generates the sink flow, such as an immersed tube, is often idealized as a point sink in theoretical studies of the hump-to-spout transition dynamics [8]. However, the external flow profile outside a tube affects which part of the flow domain gets entrained [9]. Moreover, for a fixed withdrawal flow rate Q_0 , the entrainment of both liquids can be achieved by reducing the tube-interface distance H until Q_0 reaches a critical flow rate Q_0^* . Below Q_0^* , simultaneous withdrawal of both phases is not possible at any H . To the best of our knowledge, within the reports in the selective withdrawal literature, it remains to understand how the presence of a tube affects the entrainment flow rate of each phase and how Q_0^* is controlled by the liquid and tube properties.

In this Letter, we study fluid entrainment by selective withdrawal with a tube in its full range of independent parameters that begins from a thin jet and ends when the jet fills the whole capillary tube. From a practical perspective, tube-based selective withdrawal has been applied to particle and cell coatings [10,11]. It also arises during the manual pipette operation of a stratified liquid in blood fractionation [12] and biomolecule extraction [13]. The phenomenon could also potentially be used to form jets or droplets without microfabrication for a wide range of applications [14–17]. Thus, understanding the phase map, and dependence on material properties, as we do here, may make possible new applications.

The schematic of the setup and the definition of parameters are shown in Fig. 1. An aqueous-two-phase system (ATPS) is made by mixing a solution made of 25 wt % isopropanol and 15 wt % dipotassium phosphate. The solution will spontaneously separate in 30 min into a more dense (bottom) phase and a less dense (top) phase. The liquid is placed in a large tank (20 cm by 20 cm by 20 cm) and the bottom phase is at least 10 cm deep to minimize wall effects. The top and bottom solutions have viscosities μ_1, μ_2 and densities ρ_1, ρ_2 , respectively. The viscosity ratio $\lambda = \mu_2/\mu_1$ is no more than one in all experiments. The interfacial tension between the two phases is γ . In the experiments we also use immiscible two-phase systems that include 1-decanol (top)–glycerol aqueous solution (bottom) and glycerol aqueous solution (top)–fluorocarbon oil (bottom, 3M Novec Engineered Fluid HFE-7500).

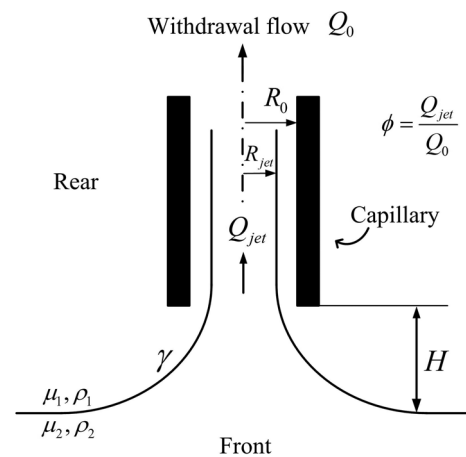


FIG. 1. Schematic of experimental setup and definition of the variables. $H > 0$ is indicated here. $H < 0$ corresponds to the end of the tube being in the lower phase. The “front” and “rear” refer to the front and rear of the capillary.

The glycerol solutions allow us to tune the viscosity from 10 to 1000 mPa s. All chemicals except otherwise specified were purchased from Sigma-Aldrich.

The circular glass capillary has inner radius R_0 and is placed perpendicular to a liquid interface with a separation distance H from the undisturbed flat interface. H is negative when the orifice is below the undisturbed interface. Capillaries with $R_0 = 150, 350, \text{ or } 750 \mu\text{m}$ are used. To minimize the influence of the capillary wall [11], the capillary wall thickness is no more than $0.67R_0$. A withdrawal flow rate Q_0 is applied to the glass capillary with a syringe pump (Harvard Apparatus). Images are taken with a digital camera through a microscope objective. When entrainment occurs, a spout of radius R_{jet} forms inside the capillary for the two-phase system (Fig. 1).

In a general case of a selective withdrawal experiment, depending on the phases being withdrawn, the parameter space of H and Q_0 is divided into three regimes: only withdrawal of the top phase (T) [Fig. 2(a)], only withdrawal of the bottom phase (B) [Fig. 2(d)], or entrainment of both phases (E) [Figs. 2(b) and 2(c)] as shown in Fig. 2(e). The transitional H and Q_0 between the T and E regimes follows a power law of $Q_0 \propto H^{3.33}$ for the ATPS system, consistent with the results reported experimentally by Cohen in aqueous-oil systems ($Q_0 \propto H^{3.4 \pm 0.6}$, $\lambda = 0.83$, $\gamma = 31 \text{ mN/m}$ [2,3]). This hump-to-spout transition has been well studied experimentally, typically by fixing H and varying Q_0 . We note that a hysteresis region exists at low flow rates above the boundary between the T and E regions where, after reducing H and triggering entrainment, the entrainment does not immediately stop if H is then slightly increased [2], as shown by the dashed line in Fig. 2(e). Similarly, hysteresis occurs between the T - B and B - E boundaries due to wetting effects.

We focus on the transitions indicated by the solid curves in Fig. 2(e) that are recorded with monotonically decreasing H . We are not aware of the phase diagram in Fig. 2(e) being recorded previously. In this figure, the flow rate Q_0^* corresponds to the Q_0 at the triple point among the T , E , and B regimes, which we will study in detail near the end of this Letter.

In the E regime, the entrainment ratio $\phi = Q_{\text{jet}}/Q_0$ increases from 0 to 1 from the TE boundary to the BE boundary; Q_{jet} is the flow rate of the bottom phase. To calculate ϕ , the width of the jet R_{jet} is measured. The calculation of the jet flow rate Q_{jet} is determined assuming fully developed laminar flow inside the capillary:

$$\phi = \frac{Q_{\text{jet}}}{Q_0} = 1 - \frac{(R_0^2 - R_{\text{jet}}^2)^2}{\left(\frac{\mu_1 R_{\text{jet}}^4}{\mu_2} - R_{\text{jet}}^4 + R_0^4\right)}. \quad (1)$$

Inclusion of the buoyancy effect for the flow in the capillary shows only a small difference with the result from Eq. (1), thus gravity is neglected in the calculation of Q_{jet} .

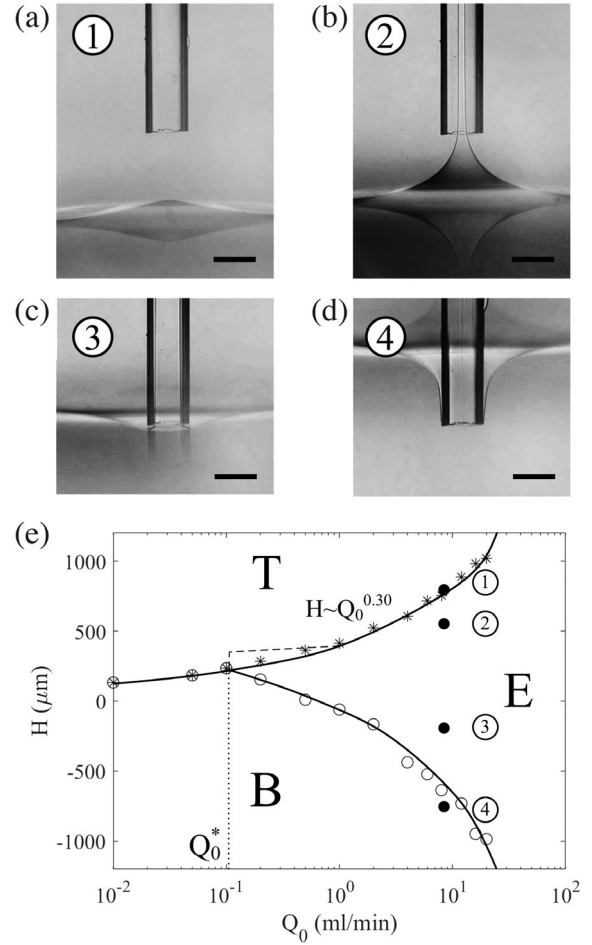


FIG. 2. The phase diagram of selective withdrawal using ATPS with $R_0 = 150 \mu\text{m}$. The numbers in (a)–(d) indicate the sampling location in (e) with corresponding numbers. (a) Only withdrawal of the top phase (T). (b) Entrainment (E) of both phases at positive H . (c) Entrainment (E) of both phases at negative H . (d) Only withdrawal of the bottom phase (B). Scale bar is $400 \mu\text{m}$ and $Q_0 = 8 \text{ ml/min}$ for (a)–(d). (e) Phase diagram on the H - Q_0 plane. T : only withdrawal of the top phase; B : only withdrawal of the bottom phase; E : entrainment of both phases. Q_0^* is the minimum flow rate of the entrainment regime. The dashed line delineates the boundary of the hysteresis region between T and E . Typical error bars are the size of the symbols. Data points were obtained by fixing Q_0 and monotonically decreasing H . The solid lines fit the data points.

To sample the phase space across the E regime in Fig. 2(e), for each fixed flow rate, the capillary is moved from top to bottom across the fluid interface (decreasing H) until both the T and B regimes are reached.

We report ϕ versus H for different Q_0 using a capillary with $R_0 = 150 \mu\text{m}$ in Fig. 3(a). We observe that ϕ varies approximately linearly with H , with the linear regression $R^2 > 0.98$ for all flow rates tested.

To rationalize the data, we adopt the analysis framework described by Lister for low-Reynolds-number flows [8]. The selective withdrawal problem of a point sink with fluids of equal viscosities can be fully characterized by two

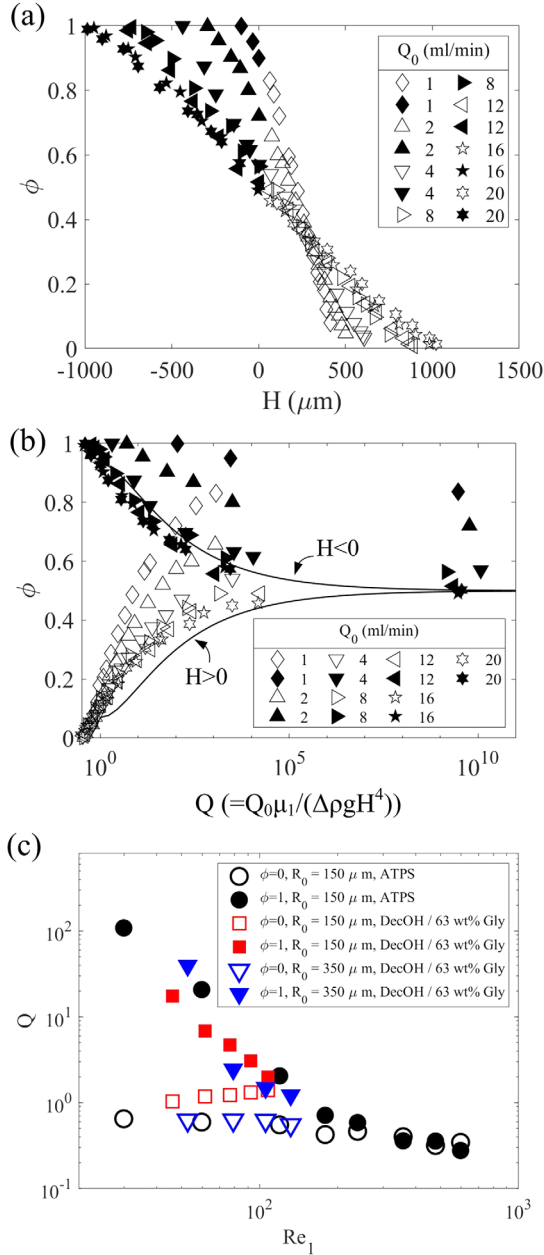


FIG. 3. (a) Entrainment ratio ϕ versus capillary height H using a capillary with $R_0 = 150 \mu\text{m}$ in ATPS system. Filled symbols represent $H < 0$ and hollow symbols represent $H > 0$. (b) ϕ versus Q for the same data in (a). Black lines are the simulation result reported by Lister (Eq. 6.4 in Ref. [8]). (c) Q versus Re_1 at $\phi = 0$ and $\phi = 1$ for the ATPS and 1-decanol (top)–63 wt% glycerol aqueous solution (bottom) on the boundary of the E regime. ATPS: $\mu_1 = 3.41 \text{ mPa}\cdot\text{s}$, $\mu_2 = 2.86 \text{ mPa}\cdot\text{s}$, $\gamma = 0.30 \text{ mN/m}$, $\Delta\rho = 310 \text{ kg/m}^3$; 1-decanol–63 wt% glycerol–water: $\mu_1 = \mu_2 = 12.0 \text{ mPa}\cdot\text{s}$, $\gamma = 5.0 \text{ mN/m}$, $\Delta\rho = 330 \text{ kg/m}^3$.

dimensionless numbers in the low-Reynolds-number limit: dimensionless withdrawal strength $Q = Q_0 \mu_1 / (\Delta \rho g H^4)$ and Bond number, $\mathcal{B} = \Delta \rho g H^2 / \gamma$, where $\Delta \rho = \rho_2 - \rho_1$. In the limit with zero surface tension, ϕ is only a function of Q for nonzero H .

The entrainment ratio is plotted versus Q in Fig. 3(b). Q reaches maximum values when $H \rightarrow 0$, which separates the upper branch of the curve where H is negative (filled symbols) and the lower branch where H is positive (open symbols). For each Q_0 , the data fall on separate curves on the ϕ - Q plane at low Q_0 , but collapse on the same curve at high Q_0 . The limiting ϕ - Q relationship at high Q_0 agrees well with the simulation result by Lister for the zero surface tension limit [8], shown as the solid curves in the figure. The simulation branch for $H < 0$ is symmetrical to the branch for $H > 0$ with respect to $\phi = 1/2$ for $\mathcal{B} \rightarrow \infty$ and equal viscosity fluid systems. The analysis [8] shows that flow is viscously driven outside a distance $\ell = O(\rho_1 Q_0 / \mu_1)$ away from the sink. Within a distance ℓ the flow becomes a momentum dominated radial flow.

Why does the experiment with a tube and the simulation with a point sink result in a different ϕ - Q relationship at lower Q_0 in Fig. 3(b)? The finite Bond number (surface tension) in the experiments cannot explain this discrepancy at lower Q_0 . The restoring force from surface tension reduces ϕ for a fixed Q with $H > 0$ and increases ϕ for $H < 0$, resulting in a right-shifted ϕ - Q relationship. From Fig. 3(b), however, ϕ is larger in the experiments than in the simulation for $H > 0$. Additionally, the experiments show asymmetry with respect to $\phi = 1/2$, which cannot be explained based on surface tension.

The only other possibility to explain the ϕ - Q relationship in the experiment at lower Q_0 is the different upstream flow profile of the tube compared to a point sink. In an ideal point sink, the flow is always radial in its vicinity, drawing fluids equally from all directions. For a capillary tube, however, the fluid it withdraws depends on the Reynolds number [9]. We define the Reynolds number as $Re_1 = \rho_1 Q_0 / (\mu_1 R_0)$. At $Re_1 = 1$ the fluid mainly enters directly from the front of the tube as a result of the viscous effects near the wall. At $Re_1 = 100$, the momentum of the fluid is significant so that the flow becomes more radial and more fluid from the rear of the tube can be withdrawn [9], which better approximates an ideal point sink.

We hypothesize that in a tube-based selective withdrawal, besides the dimensionless Q that regulates ϕ as in a point sink, Re_1 also influences ϕ through changing the external flow profile. Because ϕ as a function of H has a simple linear relationship for all Q_0 [Fig. 3(a)], we plot Q versus Re_1 at $\phi = 0$ and 1, as shown in Fig. 3(c). The result agrees with the findings inferred from [9]: beyond Re_1 of about 300, the Q values for $\phi = 0$ and 1 converge, suggesting a symmetrical relationship when the capillary is placed above or below the interface that can only result from a radial external flow around the tube. In another fluid system with four times the viscosities and 16 times the interfacial tension of the ATPS system, the Q values for $\phi = 1$ collapses with the ATPS system as a function of Re_1 . In another fluid system with $\lambda = 0.08$, $\gamma = 6.0 \text{ mN/m}$ (data not shown) the Q values converge earlier at $Re_1 = 60$.

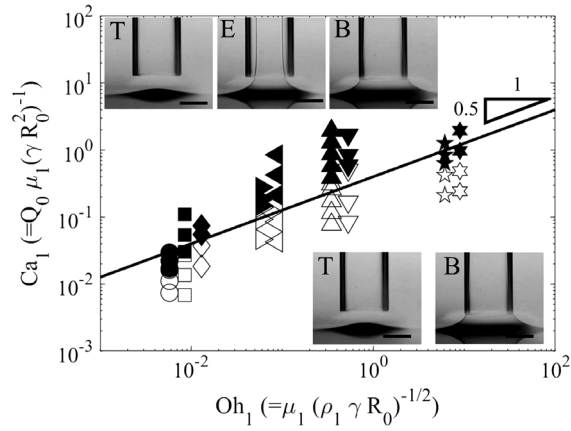


FIG. 4. Ca_1 versus Oh_1 . The black line indicates the relationship $Ca_1 = 0.38Oh_1^{1/2}$. The insets show representative time sequences when the capillary is moved toward the interface. Scale bar $500 \mu\text{m}$. Top panels represent the filled upward-pointing triangle where the E regime occurs between the T and B regimes ($Q_0 = 0.25 \text{ ml/min}$); bottom panels represent the open upward-pointing triangle where the withdrawal will jump from T to B regimes without going through entrainment of both fluids ($Q_0 = 0.20 \text{ ml/min}$). Circle, square, and diamond: $\gamma = 40 \text{ mN/m}$, $\lambda = 1$, $R_0 = 750 \mu\text{m}$, $350 \mu\text{m}$, $150 \mu\text{m}$, respectively. Right-pointing triangle and left-pointing triangle: $\gamma = 32 \text{ mN/m}$, $\lambda = 0.1$, $R_0 = 750 \mu\text{m}$, $350 \mu\text{m}$, respectively. Upward-pointing triangle and downward-pointing triangle: $\gamma = 0.3 \text{ mN/m}$, $\lambda = 1$, $R_0 = 350 \mu\text{m}$, $150 \mu\text{m}$, respectively. Pentagram and hexagram: $\gamma = 28 \text{ mN/m}$, $\lambda = 0.001$, $R_0 = 750 \mu\text{m}$, $350 \mu\text{m}$, respectively.

We note that the analysis by Lister is conducted under the assumption that $\ell \ll H$. The agreement on the ϕ - Q relationship between the low-Reynolds-number simulation and our experimental results at high Re_1 suggests that the assumption can be relaxed.

In Fig. 2(e), Q_0^* controls the minimum Q_0 for the entrainment (E) regime. Because the entrainment cannot be obtained by decreasing H at Q_0^* , gravity is a subordinate factor. A more important factor that affects Q_0^* is the restoring force from the surface tension. When the fluid forms a jet in the capillary, the typical viscous stress from the top phase $\mu_1 Q_0 / R_0^3$ has to overcome the minimum downward capillary pressure γ / R_0 . The ratio of the two stresses is the capillary number $Ca_1 = Q_0 \mu_1 / (\gamma R_0^2)$. A third factor is the flow profile around the capillary that depends on Re_1 . At small Re_1 only the fluid from the front of the capillary enters the tube, which is occupied by the bottom phase when the tube is close to the interface. Together, Ca_1 and Re_1 regulate the value of Q_0^* . For better presentation of the data we use the Ohnesorge number ($Oh_1 = \sqrt{Ca_1 / Re_1} = \mu_1 / \sqrt{\rho_1 \gamma R_0}$) instead of Re_1 .

To confirm our analysis, we measured Q_0^* in a range of different fluids and capillaries. The experimental entrainment results obtained using fluids with varying γ , μ_1 , and viscosity ratio μ_2 / μ_1 , are reported as a function of Ca_1 and

Oh_1 in Fig. 4. The evolution of the interface as H decreases is shown in the insets of Fig. 4. The top panels represent the filled symbols, and the bottom panels represent the open symbols. Four fluid systems are used in Fig. 4 with γ ranging from 0.3 to 40 mN/m and μ_1 ranging from 1 to 1000 mPa s, while μ_2 is kept constant at 1 mPa s, so that $10^{-3} < \lambda < 1$. The sole involvement of the top phase in the scaling relationship in Eq. (2) indicates the dominant effect of the top phase properties in the range of λ tested.

We take the transition flow rate Q_0^* , indicative of the triple point in Fig. 2(e), as the middle point between the nearest open and closed symbols of each type. Q_0^* is fitted as a power law of Oh_1 :

$$Ca_1^* = \frac{Q_0^* \mu_1}{\gamma R_0^2} = c Oh_1^\alpha. \quad (2)$$

The prefactor is found to be $c = 0.38 \pm 0.08$ and the exponent $\alpha = 0.50 \pm 0.07$. Equation (2) is plotted as the solid line in Fig. 4. Rearranging Eq. (2) leads to a dimensional expression for Q_0^*

$$Q_0^* = 0.38 \frac{\gamma^{3/4} R_0^{7/4}}{\rho_1^{1/4} \mu_1^{1/2}}, \quad (3)$$

where decimals are expressed in the simplest fractions for clarity. For the fluids and capillaries tested in Fig. 4, the value of Q_0^* ranges from 0.05 to 25 ml/min while H at Q_0^* stays in a small range between 200–400 μm . The Bond number stays between $0.01 < \mathcal{B} < 1$, indicating the dominant or comparable influence of surface tension to gravity near Q_0^* . It is thus reasonable to neglect gravity as a first-order approximation.

In this Letter, we demonstrate that once the flow near the tube becomes nearly radial beyond Reynolds number of 100, the entrainment flow from the tube effectively behaves like a point sink even when $R_0 > H$. Where the T - E , T - B , and E - B borders meet in the complete H - Q_0 phase diagram, analogous to a thermodynamic triple point, a critical withdrawal flow rate Q_0^* is identified. Further research is needed to investigate the coupling between the viscous stress and the region of influence near Q_0^* and the entrainment flow rate influenced by λ .

This work is supported by NSF Grant No. CMMI-1661672 and the Hong Kong RGC Research Impact Fund No. R7072-18. We thank E. Yu for help with the image processing and A. Pahlavan for helpful discussions.

*Corresponding author.
hastone@princeton.edu

- [1] S. Courrech du Pont and J. Eggers, *Phys. Rev. Lett.* **96**, 034501 (2006).
- [2] I. Cohen and S. R. Nagel, *Phys. Rev. Lett.* **88**, 074501 (2002).

-
- [3] I. Cohen, *Phys. Rev. E* **70**, 026302 (2004).
[4] S. Chaieb, [arXiv:physics/0404088](https://arxiv.org/abs/physics/0404088).
[5] F. Blanchette and W. W. Zhang, *Phys. Rev. Lett.* **102**, 144501 (2009).
[6] S. C. Case and S. R. Nagel, *Phys. Rev. Lett.* **98**, 114501 (2007).
[7] M. K. Berkenbusch, I. Cohen, and W. W. Zhang, *J. Fluid Mech.* **613**, 171 (2008).
[8] J. R. Lister, *J. Fluid Mech.* **198**, 231 (1989).
[9] A. C. True and J. P. Crimaldi, *Phys. Rev. E* **95**, 053107 (2017).
[10] I. Cohen, H. Li, J. L. Houglund, M. Mrksich, and S. R. Nagel, *Science* **292**, 265 (2001).
[11] J. Psihogios, V. Benekis, and D. Hatzivramidis, *Chem. Eng. Sci.* **138**, 516 (2015).
[12] J. Houbiers, A. Brand, L. Van de Watering, C. van de Velde, J. Hermans, P. Verwey, A. Bijnen, P. Pahlplatz, M. E. Schattenkerk, T. Wobbles *et al.*, *Lancet* **344**, 573 (1994).
[13] P. Chomczynski and N. Sacchi, *Nat. Protoc.* **1**, 581 (2006).
[14] J. Nunes, S. Tsai, J. Wan, and H. A. Stone, *J. Phys. D* **46**, 114002 (2013).
[15] Z. Pan, Y. Men, S. Senapati, and H.-C. Chang, *Biomicrofluidics* **12**, 044113 (2018).
[16] J. C. Stachowiak, D. L. Richmond, T. H. Li, A. P. Liu, S. H. Parekh, and D. A. Fletcher, *Proc. Natl. Acad. Sci. U.S.A.* **105**, 4697 (2008).
[17] P. Zhu and L. Wang, *Lab Chip* **17**, 34 (2017).